

# The MINOS experiment: results and prospects

---

J.J. Evans,<sup>a,1</sup>

<sup>a</sup>*University of Manchester,*

*Department of Physics and Astronomy, Oxford Road, Manchester, M13 9PL, United Kingdom*

*E-mail:* [justin.evans@hep.manchester.ac.uk](mailto:justin.evans@hep.manchester.ac.uk)

ABSTRACT: The MINOS experiment has used the world's most powerful neutrino beam to make precision neutrino oscillation measurements. By observing the disappearance of muon neutrinos, MINOS has made the world's most precise measurement of the larger neutrino mass splitting, and has measured the neutrino mixing angle  $\theta_{23}$ . Using a dedicated antineutrino beam, MINOS has made the first direct precision measurements of the corresponding antineutrino parameters. A search for  $\nu_e$  and  $\bar{\nu}_e$  appearance has enabled a measurement of the mixing angle  $\theta_{13}$ . A measurement of the neutral-current interaction rate has confirmed oscillation between three active neutrino flavours. MINOS will continue as MINOS+ in an upgraded beam with higher energy and intensity, allowing precision tests of the three-flavour neutrino oscillation picture, in particular a very sensitive search for the existence of sterile neutrinos.

---

<sup>1</sup>For the MINOS collaboration.

---

## Contents

<b>1</b>	<b>Introduction</b>	<b>1</b>
<b>2</b>	<b>The MINOS experiment</b>	<b>2</b>
<b>3</b>	<b>Neutrino interactions in the MINOS detectors</b>	<b>5</b>
3.1	Charged-current $\nu_\mu$ and $\bar{\nu}_\mu$ interactions	6
3.2	Charged-current $\nu_e$ interactions	7
3.3	Neutral-current interactions	9
3.4	Atmospheric neutrinos	9
<b>4</b>	<b>Muon neutrino disappearance</b>	<b>10</b>
<b>5</b>	<b>Muon antineutrino disappearance</b>	<b>12</b>
<b>6</b>	<b>Electron neutrino appearance</b>	<b>14</b>
<b>7</b>	<b>Neutral-current interaction rate</b>	<b>16</b>
<b>8</b>	<b>The Future: MINOS+</b>	<b>17</b>
<b>9</b>	<b>Conclusion</b>	<b>18</b>

---

## 1 Introduction

The MINOS experiment, as an idea, was conceived in the late 1990s [1]. This was a very important period in neutrino oscillation physics. For thirty years, results from Homestake [2] and the gallium experiments [3, 4], through to a number of atmospheric neutrino detectors [5–10], had shown that neutrinos behaved in an odd fashion, often showing significant deficits from the expected flux; but none had conclusively determined the mechanism responsible. Then, in 1998, Super-Kamiokande [11] proved decisively that muon neutrinos produced in the Earth’s atmosphere disappeared as they traveled. Around three years later, the SNO experiment showed conclusively that neutrinos, as they propagated, changed between their three flavours [12]. This discovery of neutrino flavour change showed that neutrinos had mass and did not conserve lepton number; it was the first, and still the only, observation of physics beyond the Standard Model.

It was during this period of discovery that the MINOS experiment was proposed, to begin an era of precision measurement of this new phenomenon. The data at the time were well modeled by the theory of neutrino oscillation, in which the rate of oscillation between the three flavours is governed by the differences between the squared neutrino masses,  $\Delta m_{21}^2$ .

and  $\Delta m_{32}^2$ . The magnitude of the flavour change is governed by three mixing angles,  $\theta_{12}$ ,  $\theta_{23}$  and  $\theta_{13}$ , and a  $\mathcal{CP}$ -violating phase  $\delta$ ; these parameters form the PMNS rotation matrix [13] that relates the neutrino mass eigenstates to the flavour eigenstates. Nature has decreed that the two mass splittings differ by more than an order of magnitude, and that one of the mixing angles,  $\theta_{13}$ , is small. Therefore, oscillation phenomenology can be divided into two distinct regimes: ‘solar’ oscillation driven by  $\Delta m_{21}^2$  and  $\theta_{12}$ , and ‘atmospheric’ oscillation driven by  $\Delta m_{32}^2$  and  $\theta_{23}$ . MINOS was designed to make precision measurements of the parameters governing the atmospheric oscillation regime; however, it has also played an important role in the measurement of  $\theta_{13}$  and will, in the future, make sensitive searches for the existence of sterile neutrinos. An important feature of the MINOS design is the ability of the detectors to identify both  $\nu_\mu$  and  $\bar{\nu}_\mu$  interactions separately. This has allowed MINOS to make the first direct precision tests that neutrinos and antineutrinos obey the same oscillation parameters in the atmospheric regime [14–17].

To achieve its goals, the MINOS experiment uses the world’s most powerful neutrino beam, the NuMI beam. In making best use of this beam, the experiment has pioneered the two-detector technique, which is now the gold standard for all neutrino oscillation experiments.

## 2 The MINOS experiment

The NuMI facility [18] provides MINOS with an intense beam of muon flavoured neutrinos at energies of a few GeV. The atmospheric neutrino mass splitting drives oscillation between muon and tau flavour neutrinos, with an energy dependence given by

$$P(\nu_\mu \rightarrow \nu_\mu) = 1 - \sin^2(2\theta) \sin^2 \left( \frac{1.27 \Delta m^2 [\text{eV}^2] L [\text{km}]}{E [\text{GeV}]} \right). \quad (2.1)$$

In this two-flavour approximation,  $\Delta m^2$  is an admixture of  $\Delta m_{32}^2$  and  $\Delta m_{31}^2$ ;  $\theta$  is also an admixture of the mixing angles, but is heavily dominated by  $\theta_{23}$ . Since MINOS cannot observe the  $\nu_\tau$  appearance, it is the measurement of this  $\nu_\mu$  survival probability that is used to determine the parameters  $\theta$  and  $\Delta m^2$  [17, 19–22].

A non-zero  $\theta_{13}$  causes a small amount of  $\nu_e$  appearance in the beam, with an energy dependence given by

$$P(\nu_\mu \rightarrow \nu_e) \approx \sin^2(\theta_{23}) \sin^2(2\theta_{13}) \sin^2 \left( \frac{1.27 \Delta m^2 [\text{eV}^2] L [\text{km}]}{E [\text{GeV}]} \right). \quad (2.2)$$

MINOS has selected a sample of  $\nu_e$ -enhanced events to make a measurement of  $\theta_{13}$  [23–26].

An important signature of neutrino oscillation is that the rate of neutral-current (NC) neutrino interactions is unchanged by the process. The NC interaction is equally sensitive to all three neutrino flavours, so this proves that flavour change is occurring between the three active neutrino flavours. By analysing NC interactions, MINOS has confirmed that oscillation is the correct picture, and has shown no evidence that this oscillation includes additional, sterile neutrino flavours [27–29].

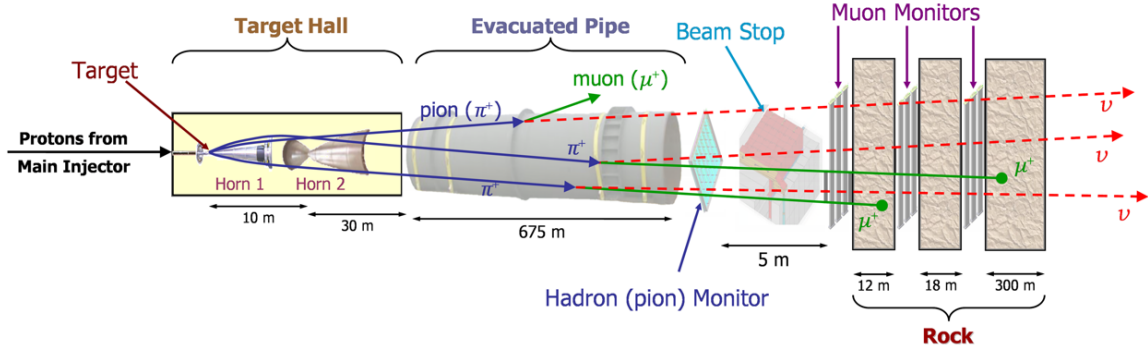


Figure 1. The NuMI beam.

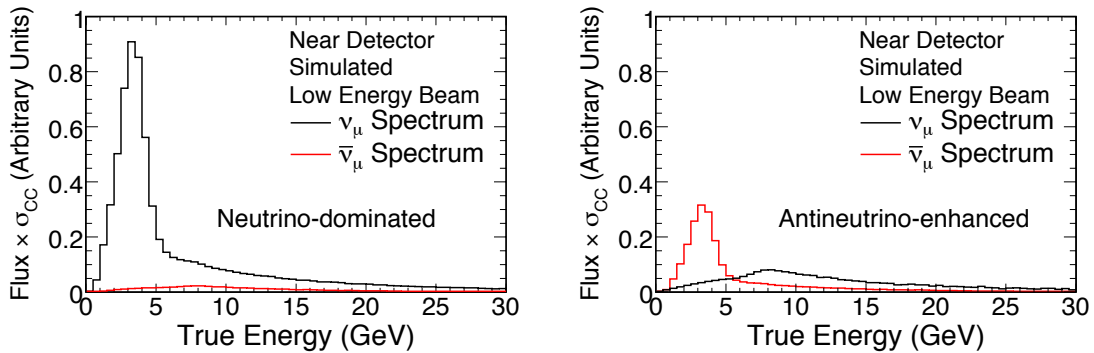
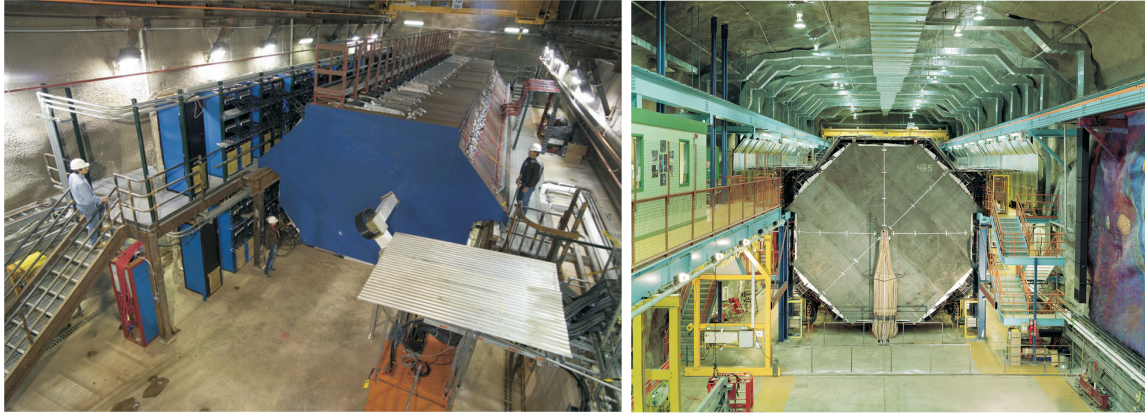


Figure 2. The composition of the NuMI beam, when configured to produce (left) a neutrino-dominated beam and (right) an antineutrino-enhanced beam.

The NuMI beam [18], based at Fermilab in Chicago, has run since 2005 and has reached a typical beam power of 350 kW. The Fermilab Main Injector produces a  $10 \mu\text{s}$  pulse of around  $3 \times 10^{13}$  protons every 2.2 s. These protons have an energy of 120 GeV and strike a graphite target, as shown in Figure 1. This target has a length of 2.0 nuclear interaction lengths and consists of a series of forty-seven 2 cm long graphite fins, separated by 0.3 mm. A shower of hadrons is produced at the target, consisting primarily of pions with a significant kaon component at higher energies. These hadrons pass through two parabolic, magnetic horns which focus either positive or negative hadrons depending on the direction of the electric current through the horns. The focused hadrons pass down a 675 m long, helium filled pipe, in which they decay to produce a beam of predominantly muon flavoured neutrinos, with a small electron neutrino component from the decays of muons and kaons.

Figure 2 shows the composition of the NuMI beam. With the horns configured to focus positive hadrons, the observed beam consists of 91.7%  $\nu_\mu$ , 7.0%  $\bar{\nu}_\mu$  and 1.3%  $\nu_e$  and  $\bar{\nu}_e$ . With the horns focusing negative hadrons, the observed beam consists of 39.9%  $\bar{\nu}_\mu$ , 58.1%  $\nu_\mu$  and 2.0%  $\nu_e$  and  $\bar{\nu}_e$ . The significant difference in composition and event rate between these two configurations arises mainly from the fact that the  $\bar{\nu}_\mu$  interaction cross section is a factor of between two and three lower than the  $\nu_\mu$  interaction cross section.

The neutrino beam peaks at an energy of close to 3 GeV. However, the current through



**Figure 3.** The MINOS detectors. Left: the Near Detector at Fermilab; right: the Far Detector at the Soudan Underground Laboratory.

the focusing horns and the relative positions of the horns and target are variable, allowing the energy of the beam peak to be varied to as high as 10 GeV. This feature has enabled MINOS to study and understand the beam in detail [30], improving the simulation of the beam beyond the raw Fluka [31] and GEANT [32, 33] Monte Carlos, and significantly reducing the systematic uncertainty from the modeling of the neutrino flux.

A total of  $10.56 \times 10^{20}$  protons on target of beam data has been analysed in the neutrino-dominated beam mode; an additional  $0.15 \times 10^{20}$  protons on target of data with a 10 GeV beam peak has also been used. In the antineutrino-enhanced beam mode, a total of  $3.36 \times 10^{20}$  protons on target of beam data has been analysed.

The two MINOS detectors [34] are steel-scintillator calorimeters, shown in Figure 3. They consist of planes of inch-thick steel, interleaved with planes of 1 cm thick plastic scintillator. The scintillator planes are divided into 4 cm wide strips, as shown in Figure 4. Along the centre of each strip, a wavelength shifting fibre collects the scintillation light, shifts it to green wavelengths, and takes it out to a photomultiplier tube. Any charged particles passing through the detector deposit their energy to produce light; the pattern of these deposits allows the topology of the neutrino interaction to be reconstructed. The scintillator strips are aligned orthogonally on adjacent detector planes, to allow three dimensional reconstruction. The detectors are magnetised to around 1.3 T, allowing the charge of particles to be identified.

The smaller of the two detectors, the Near Detector (ND), sits at Fermilab, 1.04 km from the target. With a mass of 0.98 kton, it measures the energy spectra of the neutrinos before oscillation. The Far Detector is located at the Soudan Underground Laboratory in northern Minnesota, 705 m underground and 735 km from the target. With a mass of 5.4 kton, it again measures the neutrino energy spectra, seeing the appearance and disappearance of neutrinos due to oscillation.

This two-detector arrangement is very powerful in reducing systematic uncertainties. Neutrino physics is beset with uncertainty: in particular, interaction cross sections are unknown to many tens of per cents, and neutrino fluxes can be mismodeled by similar

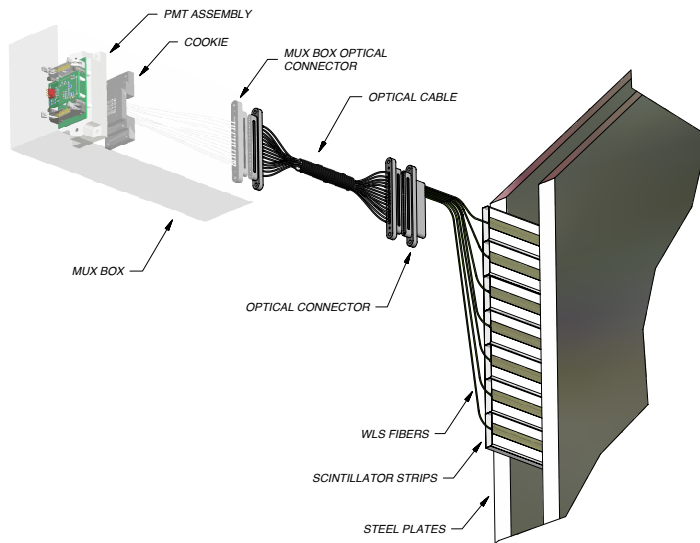


**Figure 4.** A MINOS detector plane.

amounts. However, these uncertainties affect both detectors in exactly the same way so cancel very effectively when a ratio is taken of the Near to Far Detector energy spectra. As an indication of how well this works, despite the uncertainties of tens of per cent in the simulated event rate in the detectors, once the Near to Far Detector ratio is taken, the normalization is known to 1.6%.

The MINOS Far Detector is also a very effective detector of neutrinos produced in the atmosphere. Since it was switched on in 2003, it has recorded 37.9 kton-years of data, recording 2072 candidate neutrino interactions that have been included into the analyses of the beam data to improve the precision of the oscillation parameter measurements [17, 35–37].

### 3 Neutrino interactions in the MINOS detectors

Three types of neutrino interaction, shown in Figure 5, are of interest to MINOS. Muon neutrinos and antineutrinos interact through the charged-current (CC) process

$$\nu_\mu(\bar{\nu}_\mu) + X \rightarrow \mu^{-(+)} + X'.$$

The cascade of hadrons,  $X'$ , produces a diffuse shower of energy deposits near the interaction vertex. The muon produces a long track that curves in the magnetic field, the direction of curvature identifying the incoming neutrino as a  $\nu_\mu$  or a  $\bar{\nu}_\mu$ .

All active neutrino flavours undergo NC interactions through the process

$$\nu + X \rightarrow \nu + X'.$$

Only the hadronic cascade is observed, producing a diffuse shower of energy deposits.

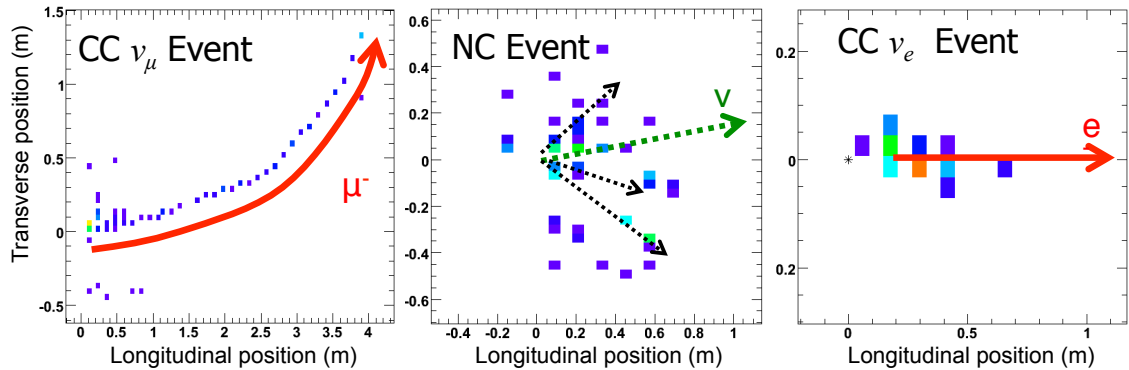


**Figure 5.** Neutrino interaction topologies observed in the MINOS detectors. Left: a CC  $\nu_\mu$  interaction. Middle: a NC interaction. Right: a CC  $\nu_e$  interaction. Each coloured rectangle represents an excited scintillator strip, the colour indicating the amount of light: purple and blue are low light levels, through to orange and red for the highest light levels.

Finally, electron neutrinos undergo CC interactions through the process

$$\nu_e + X \rightarrow e^- + X'.$$

The electron gives rise to an electromagnetic shower, which produces a much denser, more compact shower of energy deposits.

The energy of the neutrino is determined by summing the energies of the shower and any muon track. The muon energy is determined from the length of stopping tracks, leading to a resolution of around 5%, and from the curvature in the magnetic field for tracks that exit the detector, leading to a resolution of around 10%. For NC and  $\nu_e$  CC interactions, the energy of the shower is determined through calorimetry. The calorimetric energy resolution for hadronic showers is around  $55\%/\sqrt{\text{energy}}$  [38] and for electromagnetic showers  $20\%/\sqrt{\text{energy}}$  [39]. For  $\nu_\mu$  CC interactions, a more sophisticated approach is used to improve the resolution of hadronic shower energy measurement [40]. For low energy showers (of a few GeV or below), significant additional information is held in the topology of the shower. Three event characteristics are used: the calorimetric energy deposit within 1 m of the interaction vertex, the sum of the calorimetric energy in the two largest showers in the event, and the physical length of the largest shower. These variables are input into a  $k$ -nearest-neighbour algorithm [41], which finds the best matches from a library of simulated events and uses these to estimate the hadronic energy. This improves the shower energy resolution from 55% to 43% for showers between 1.0 GeV and 1.5 GeV.

### 3.1 Charged-current $\nu_\mu$ and $\bar{\nu}_\mu$ interactions

To make a measurement of  $P(\nu_\mu \rightarrow \nu_\mu)$ , it is necessary to select a pure sample of  $\nu_\mu$  CC interactions. This is achieved by selecting events with a clear muon track. The main loss in efficiency comes from events with a high inelasticity in which a short muon track is hidden in a large hadronic cascade. The main background occurs at low energies, and consists of small cascades from NC interactions in which a low energy hadron, such as a

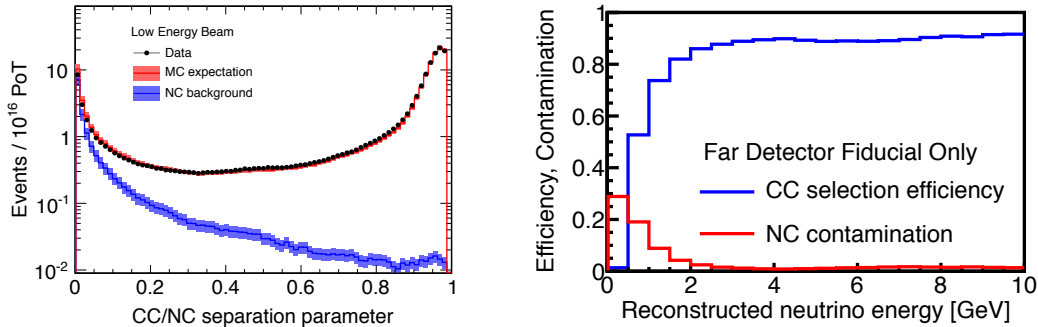


**Figure 6.** Left: the discrimination variable used to separate  $\nu_\mu$  CC interactions from hadronic backgrounds. Events with a parameter value greater than 0.3 are selected as  $\nu_\mu$  CC interactions. Right: the efficiency and background contamination of the selected  $\nu_\mu$  CC sample in the Far Detector.

proton or a charged pion, exhibits a track-like topology that mimics a low energy muon. Four variables are constructed that discriminate between muons tracks, which are typically long and show a constant energy deposition along the length, and spurious hadronic tracks, which are typically shorter and show greater fluctuations in the energy deposition. These variables are the event length, the average energy deposited per scintillator plane along the track, the transverse energy deposition profile, and the fluctuation of the energy deposition along the track. These variables are input into a  $k$ -nearest-neighbour algorithm, which calculates a single discrimination variable, shown in Figure 6 [42]. Events for which this variable is greater than 0.3 are selected as CC  $\nu_\mu$  interactions, yielding a sample with 90% efficiency; below 2 GeV, the NC contamination is 6.5%. The energy dependent efficiency and contamination are shown in Figure 6.

The CC interactions of  $\nu_\mu$  and  $\bar{\nu}_\mu$  result in very similar topologies; the  $k$ -nearest-neighbour discriminant is therefore used in the same way in both the neutrino-dominated and antineutrino-enhanced beams. When performing a direct measurement of the antineutrino oscillation parameters, an additional selection cut is made, requiring the charge of the muon track to be positive. This uses the direction of curvature of the muon as measured by a Kalman Filter algorithm [43]. A further sample of  $\bar{\nu}_\mu$  CC interactions is obtained from the 7%  $\bar{\nu}_\mu$  component in the neutrino-dominated beam. This sample contains a significant background of  $\nu_\mu$  events in which a  $\mu^-$  has been identified with the incorrect charge, often at low energies where the muon undergoes significant scattering. Therefore a much stricter set of selection criteria are applied to purify this  $\bar{\nu}_\mu$  sample [15].

### 3.2 Charged-current $\nu_e$ interactions

The selection of  $\nu_e$  CC interactions focuses on identifying the dense showers from the electromagnetic interaction of the electron, rather than the much more diffuse hadronic showers. The primary background comes from purely hadronic showers which can have a denser than average energy deposit, particularly in the presence of a neutral pion decaying to photons.



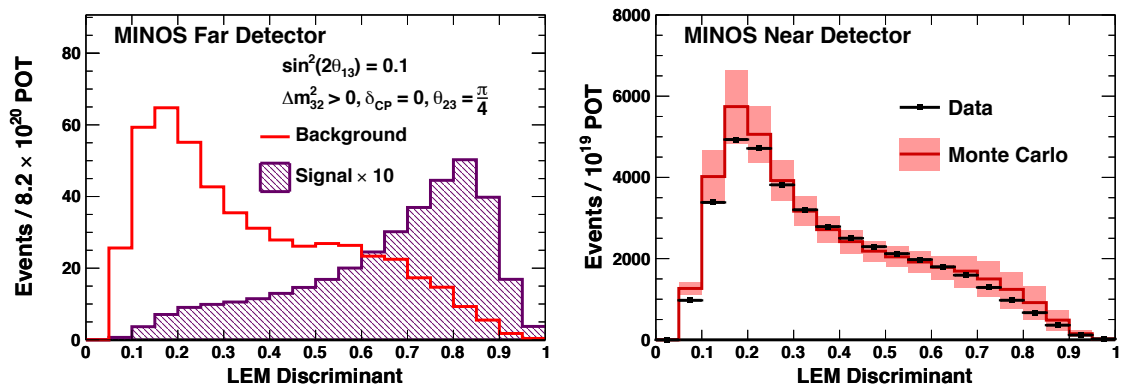


**Figure 7.** Left: the Library Event Matching discriminant, showing the expected distribution for background and CC  $\nu_e$  signal events in the Far Detector, in the neutrino-dominated beam. Note that the signal, simulated for  $\sin^2(2\theta_{13}) = 0$ ,  $\delta = 0$  and a normal mass hierarchy, has been scaled up by a factor of ten for visibility. Right: the same discriminant as observed in the Near Detector, compared with the simulated expectation.

Once a set of shower-like events in the signal region of 1–8 GeV has been obtained, a pattern matching approach, called Library Event Matching, is used to identify the interactions most likely to be  $\nu_e$  CC [44, 45]. Each event in the data is compared to a library of  $5 \times 10^7$  simulated signal and background events; its similarity to the library events is quantified by comparing the pattern of energy deposits in each scintillator strip excited by the shower, where the energy deposit is quantified by the charge recorded on the photomultiplier tube. For an arbitrary energy deposit, the mean expected charge on a photomultiplier tube will be some value  $\lambda$ . The probability of observing an amount of charge  $n$  is then a Poisson distribution,  $P(n|\lambda)$ . The likelihood,  $\mathcal{L}$ , of a data event corresponding to the same physical shower topology as a simulated library event can therefore be calculated as

$$\log \mathcal{L} = \sum_{i=1}^{N_{\text{strips}}} \log \left[ \int_0^{\infty} P(n_{\text{data}}^i|\lambda)P(n_{\text{lib}}^i|\lambda)d\lambda \right],$$

where  $i$  represents the  $i$ th scintillator strip in the shower. Using this definition of the likelihood, the 50 library events are identified that best match the data event. Three quantities are calculated from this set of 50 best-matching library events: the fraction that are true  $\nu_e$  CC events, the average inelasticity of the true  $\nu_e$  CC events, and the average fraction of charge that overlaps between the data event and each  $\nu_e$  CC library event. These three quantities are input to a neural network, which calculates a classification variable shown in Figure 7. Events with a classification variable value above 0.6 are selected for analysis.

The efficiency of the  $\nu_e$  CC selection is estimated from the data, rather than relying totally on the simulation. To obtain a pure sample of true hadronic showers a sample of well identified  $\nu_\mu$  CC events is selected, and the energy depositions corresponding to the muon track are removed [46]. The simulated energy depositions of an electron are then inserted [47], providing a realistic sample of  $\nu_e$  CC events. Using this method, the  $\nu_e$  CC

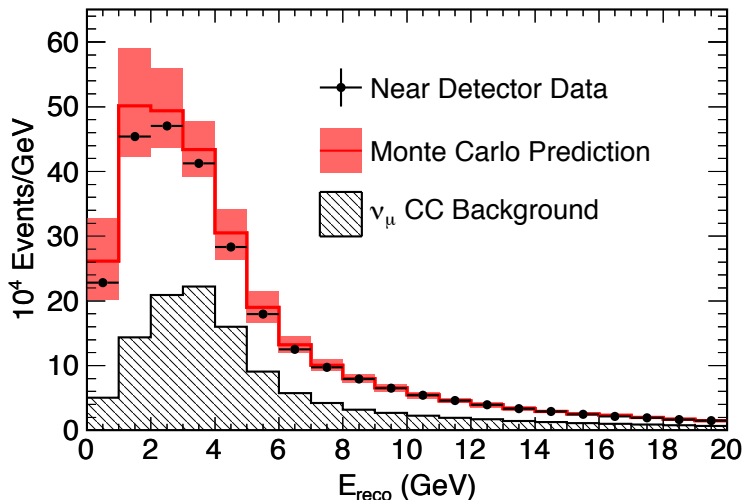


**Figure 8.** The sample of events identified as NC interactions in the Near Detector.

identification efficiency is found to be  $(57.4 \pm 2.8)\%$  in the neutrino-dominated beam, and  $(63.3 \pm 3.1)\%$  in the antineutrino-enhanced beam.

### 3.3 Neutral-current interactions

The signal of an NC interaction is a diffuse hadronic shower.  $\nu_\mu$  CC interactions also produce hadronic showers, and if the inelasticity is high, the tell-tale muon track may not visibly extend past the shower. To purify a sample of NC interactions, a simple cut-based approach is taken [48]: events are classified as NC-like if the event contains no reconstructed track, or if the track extends no more than six planes past the end of the shower. The resulting distribution of NC interactions in the Near Detector is shown in Figure 8. The NC identification efficiency is 89%, with 61% purity. This selection will identify 97% of  $\nu_e$  CC interactions as NC events; therefore an analysis of NC interactions in the FD must account for the  $\nu_e$  appearance caused by a non-zero  $\theta_{13}$ .

### 3.4 Atmospheric neutrinos

Atmospheric neutrino interactions are selected out of any activity seen in the FD outside of the  $10 \mu\text{s}$  periods when the NuMI beam is active [37]. The oscillation signal is contained in the  $\nu_\mu$  CC interactions, and as with the beam-induced interactions these are identified by the presence of a muon track.

The FD has a single-hit timing resolution of 2.5 ns. This timing information is used to determine the direction in which the detector activity is traveling. Any downwards traveling activity is required to begin well inside the detector, to eliminate cosmic muons entering from above. All upwards or horizontally traveling activity is almost certain to be neutrino-induced, since no other particle can survive through the many kilometres of rock. All activity with a zenith angle of  $\cos\theta_z < 0.14$  is defined as horizontal or down-going; this corresponds to an overburden of at least 14 km water equivalent.

From this sample of neutrino-induced activity, all events with a track crossing at least eight planes are designated track-like; all events with only shower-like activity crossing at least four planes are designated shower-like. These track-like and shower-like samples are used in the neutrino oscillation measurements. The track-like sample contains the oscillation signal of  $\nu_\mu$  disappearance. The shower-like sample contains mainly NC interactions and  $\nu_e$  and  $\bar{\nu}_e$  CC interactions; it shows little oscillation signal, but is very important for setting the normalization of the atmospheric neutrino flux.

## 4 Muon neutrino disappearance

The atmospheric oscillation parameters,  $|\Delta m^2|$  and  $\sin^2(2\theta)$ , are measured by observing and fitting the energy dependence of  $\nu_\mu$  and  $\bar{\nu}_\mu$  disappearance. To minimise the impact of systematic uncertainties, the energy spectra of the  $\nu_\mu$  and  $\bar{\nu}_\mu$  CC interactions observed in the ND (shown in Figure 9 for the neutrino-dominated beam) are used to predict the spectrum at the FD, in the absence of oscillation [20, 49]. The neutrino energy spectra at the ND and FD are not identical: the ND subtends a relatively large angle to the beam, so for each pion or kaon a range of decay angles can produce a neutrino that passes through the detector, corresponding to a range of neutrino energies. However, the FD is effectively a point when viewed from the neutrino production location, so a single decay angle for each hadron, and therefore a single neutrino energy, contributes to the flux. To take this difference into account, the hadron-decay kinematics are encoded into a beam transfer matrix that converts the observed ND flux into a predicted FD flux. Once the ND data has been used in this way, the most important systematic uncertainties are those that can affect the two detectors differently, primarily reconstruction efficiencies and miscalibrations of the neutrino energy measurement in the detectors [50]. These uncertainties are included in the fit that extracts the oscillation parameters [51].

The top row of Figure 10 shows the predicted spectra of  $\nu_\mu$  and  $\bar{\nu}_\mu$  CC interactions from the neutrino-dominated and antineutrino-enhanced beams at the FD, along with the data. In the neutrino-dominated beam, an additional sample is used, consisting of neutrinos interacting outside the fiducial volume of the detector, and in the rock surrounding the detector [52, 53]. This non-fiducial sample consists mainly of high energy neutrinos, and has significantly lower resolution as not all the energy is contained in the detector; however, it does contain some oscillation information. In all samples, a clear, energy-dependent deficit of  $\nu_\mu$  and  $\bar{\nu}_\mu$  interactions is observed. The ratio of the data to the expectation for the  $\nu_\mu$  interactions in the neutrino-dominated beam is shown in Figure 11. This ratio shows the ‘dip and rise’ energy dependence of the deficit, which is characteristic of oscillation and described by equation (2.1).

The bottom row of Figure 10 shows the spectra of atmospheric  $\nu_\mu$  and  $\bar{\nu}_\mu$  CC interactions, as a function of  $L/E$  where  $L$  is the distance traveled by the neutrino and  $E$  its energy. The atmospheric neutrino events are divided into  $\nu_\mu$  and  $\bar{\nu}_\mu$  interactions according to the direction of curvature of the muon, and separated into samples depending on whether or not the interaction vertex is contained in the detector.

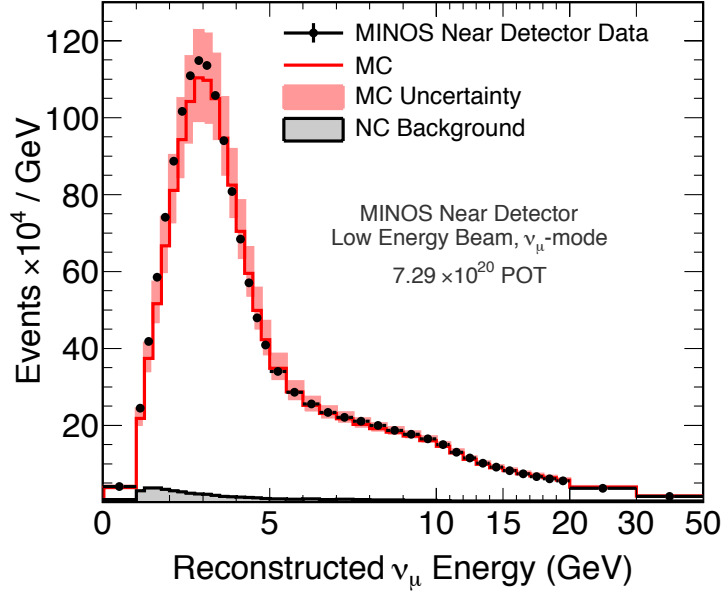


**Figure 9.** The energy spectrum of  $\nu_\mu$  CC interactions observed in the ND, compared to the simulation.

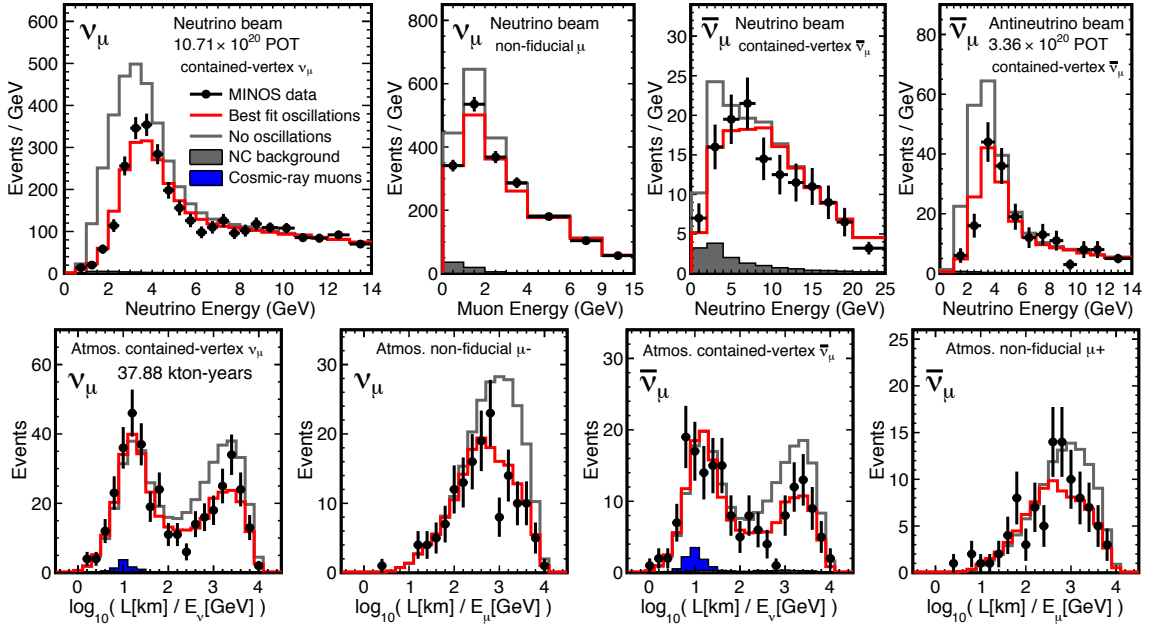


**Figure 10.** The energy spectra of  $\nu_\mu$  and  $\bar{\nu}_\mu$  CC interactions observed at the FD, compared to the expectation with and without oscillation. The top row shows beam-induced neutrinos; the bottom row shows atmospheric neutrinos.

All the observed  $\nu_\mu$  and  $\bar{\nu}_\mu$  CC interactions are fit according to equation (2.1), under the assumption that neutrinos and antineutrinos have the same oscillation parameters.

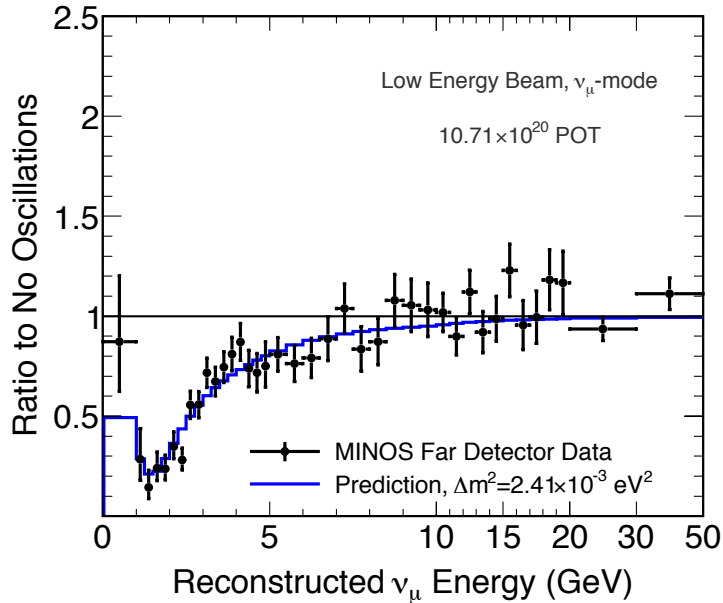


**Figure 11.** The ratio of the observed  $\nu_\mu$  energy spectrum to the expectation in the case of no oscillation, in the neutrino-dominated beam.

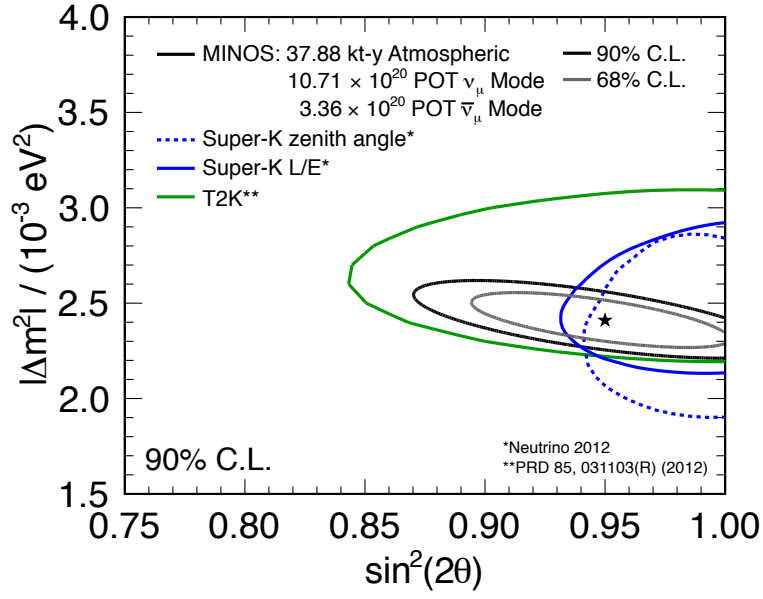
The resulting measurement of  $|\Delta m^2|$  and  $\sin^2(2\theta)$  is shown in Figure 12. The fit yields  $|\Delta m^2| = (2.41_{-0.10}^{+0.09}) \times 10^{-3} \text{ eV}^2$  and  $\sin^2(2\theta) = 0.950_{-0.036}^{+0.035}$ , disfavouring maximal mixing at the 86% confidence level. Figure 12 compares this measurement to those from Super-Kamiokande [54] and T2K [55]. The MINOS measurement is the most precise determination of  $|\Delta m^2|$ , and all measurements of  $\sin^2(2\theta)$  are consistent.

## 5 Muon antineutrino disappearance

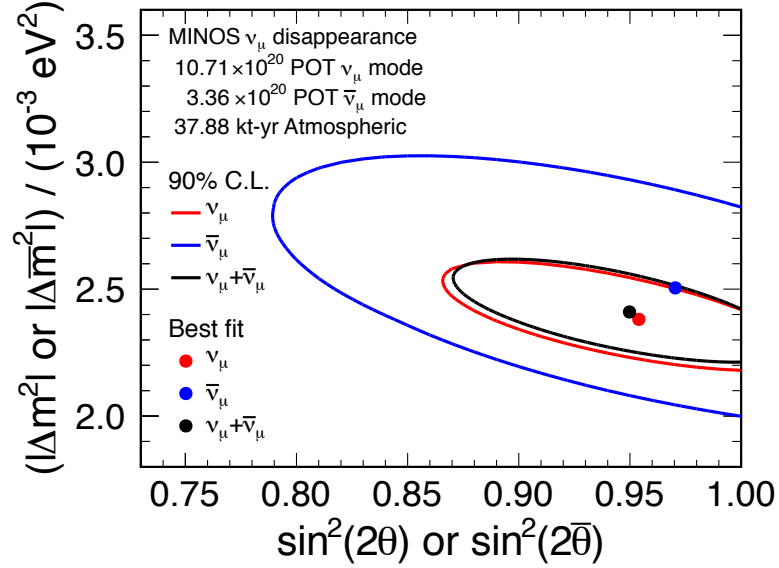
In the standard model of neutrino oscillation, neutrinos and antineutrinos obey the same parameters, with  $CPT$  symmetry requiring that the masses of particles and antiparticles are identical. The most sensitive test of this symmetry in other sectors is from the kaon system [56]. The data from the antineutrino-enhanced beam enables the first direct comparison of the neutrino and antineutrino oscillation parameters in the atmospheric region. This comparison provides a limit on non-standard interactions with the matter passed through by the neutrino beam [57–63].

Figure 10 showed the energy spectra of  $\bar{\nu}_\mu$  interactions observed in the FD. These spectra can be fit, allowing the antineutrino oscillation parameters to differ from those for neutrinos. This fit yields the antineutrino parameter measurement shown in Figure 13:  $|\Delta \bar{m}^2| = (2.50_{-0.25}^{+0.23}) \times 10^{-3} \text{ eV}^2$  and  $\sin^2(2\bar{\theta}) = 0.97_{-0.08}^{+0.03}$ . This is in excellent agreement with the parameters measured with neutrinos neutrinos alone (the red line in Figure 13).

The measured limit on the difference between the neutrino and antineutrino mass splittings is shown in Figure 14, and is  $|\Delta \bar{m}^2| - |\Delta m^2| = (0.12_{-0.26}^{+0.24}) \times 10^{-3} \text{ eV}^2$ .



**Figure 12.** The allowed regions for the atmospheric oscillation parameters  $|\Delta m^2|$  and  $\sin^2(2\theta)$ , assuming identical neutrino and antineutrino oscillation parameters. The MINOS result is compared to measurements from Super-Kamiokande [54] and T2K [55].



**Figure 13.** The allowed region for antineutrino oscillation parameters (blue line), compared to the region measured with neutrinos alone (red line) and the region measured using both neutrinos and antineutrinos under the assumption they have the same parameters (black line).

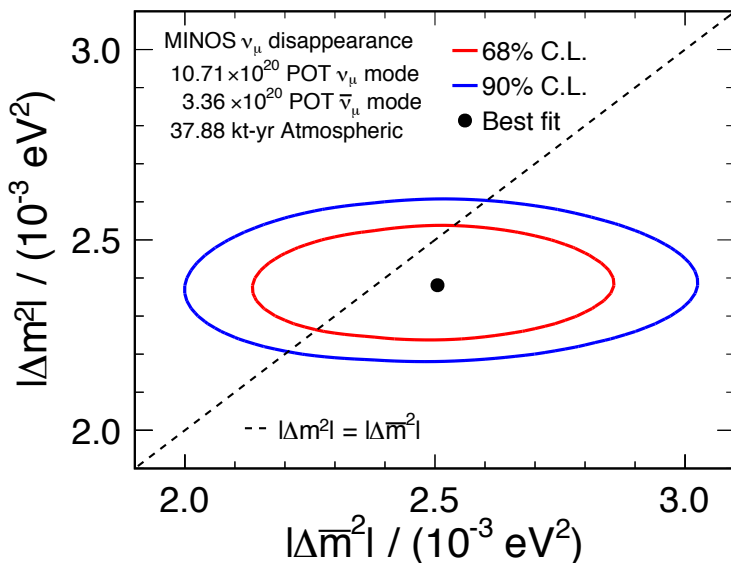


**Figure 14.** The measured limit on the difference between the mass splittings of neutrinos and antineutrinos.

## 6 Electron neutrino appearance

A search for  $\nu_e$  and  $\bar{\nu}_e$  appearance in the  $\nu_\mu$  and  $\bar{\nu}_\mu$  beams enables a measurement of the mixing angle  $\theta_{13}$ . It is critical to know the level of background to the  $\nu_e$  sample in the FD. The energy spectrum of background events measured in the ND is used to predict the spectrum expected in the FD. However, the background consists of three components: NC interactions, CC  $\nu_\mu$  and  $\bar{\nu}_\mu$  interactions, and the intrinsic  $\nu_e$  component in the beam. The relative contribution between the ND and FD is different for all of these components, since they are affected differently by oscillation, and the kinematics of the production in the beam are different. Therefore each background must be individually measured. The NuMI beam can be configured to produce neutrino beams of varying energy, by altering the current passing through the magnetic horns and changing the relative positions of the target and horns. Between these different beam configurations, the relative contributions of the three background components changes in a well understood way, as shown in Figure 15. By comparing the ND data to the simulation in the three different beam configurations shown in the figure, the contributions of the three background components can be extracted [64].

Using the data-driven background extraction procedure, a total of 127.7 background events are expected at the FD in the neutrino-dominated beam, and 17.5 events in the antineutrino-enhanced beam. In the data, 152 and 20 events are observed, respectively. Figure 16 shows the energy spectra of these events, divided into bins of the Library Event Matching discriminant variable.

The data are fit to extract a measurement of  $\theta_{13}$ . The resulting measurement is shown in Figure 17. The measured value of  $\theta_{13}$  depends on the  $\mathcal{CP}$  violating phase  $\delta$ , which directly affects the  $\nu_e$  and  $\bar{\nu}_e$  appearance probabilities, and the mass hierarchy, which affects

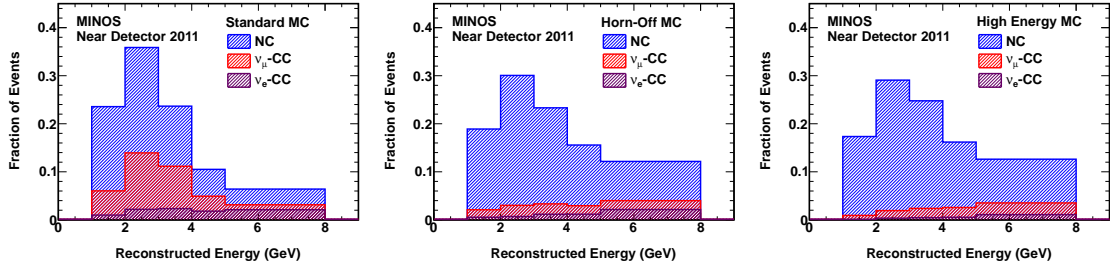


**Figure 15.** The contribution of the three components to the background in the  $\nu_e$  appearance search, as simulated in the ND. Left: the regular beam data; middle: with no current in the NuMI focusing horns; right: a high energy beam configuration.

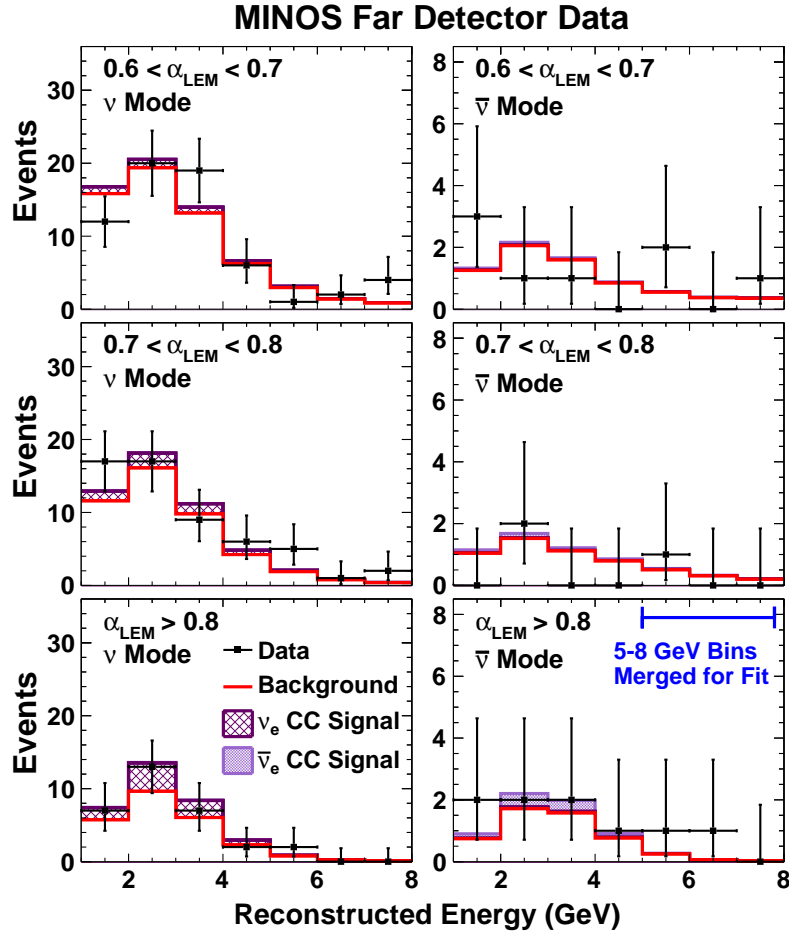


**Figure 16.** The CC  $\nu_e$  (left) and  $\bar{\nu}_e$  (right) candidate events selected in the FD, compared to the expectation without any  $\nu_e$  appearance (red) and with the best fit for  $\theta_{13}$  (purple). The events are divided into bins of the Library Event Matching discriminant variable.

the appearance probabilities through the interactions of the neutrinos with the matter in the Earth's crust. Assuming a normal mass hierarchy,  $\delta = 0$  and  $\theta_{23} < \pi/4$ , MINOS measures  $2 \sin^2(2\theta_{13}) \sin^2(\theta_{23}) = 0.051^{+0.038}_{-0.030}$ . Assuming an inverted mass hierarchy,  $\delta = 0$



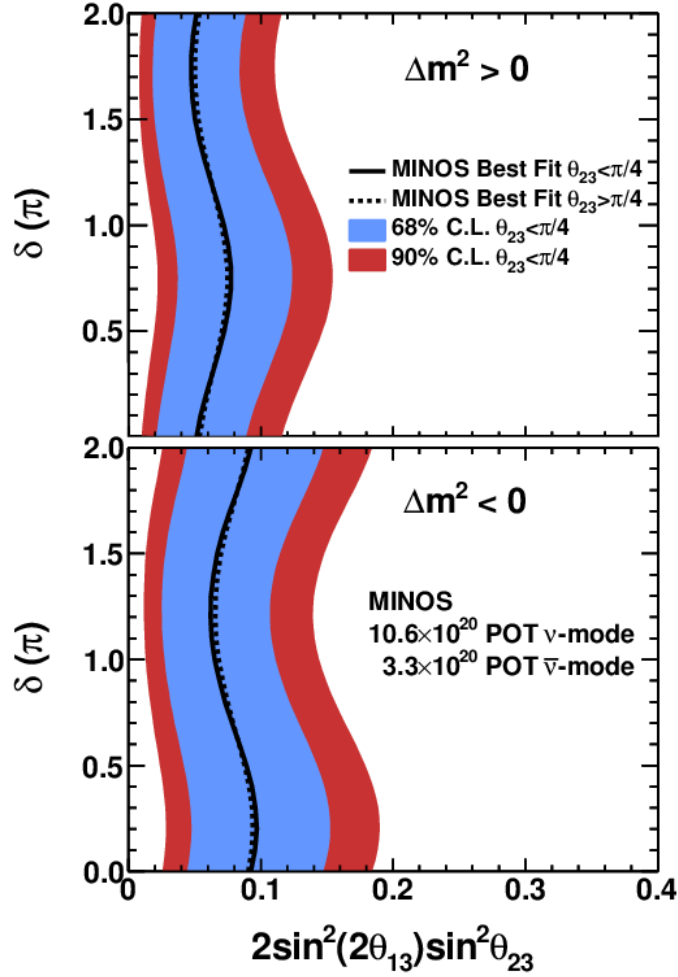


Figure 17. The allowed regions for  $2 \sin^2(2\theta_{13}) \sin^2(\theta_{23})$ .

and  $\theta_{23} < \pi/4$ , MINOS measures  $2 \sin^2(2\theta_{13}) \sin^2(\theta_{23}) = 0.093_{-0.049}^{+0.054}$ .

This MINOS measurement is the first ever search for  $\bar{\nu}_e$  appearance in a long-baseline  $\bar{\nu}_\mu$  beam, and the first search for  $\nu_e$  and  $\bar{\nu}_e$  appearance with significant matter effects. Both of these effects provide some sensitivity to the neutrino mass hierarchy and  $\mathcal{CP}$  violation. The sensitivity of MINOS to these parameters is modest, but this contributes the first analysis of the type that will be used by all future long-baseline experiments. The resulting values of the likelihood by which MINOS disfavours various values of these parameters are shown in Figure 18 [65].

## 7 Neutral-current interaction rate

The energy spectrum of NC interactions in the FD should be unchanged by standard neutrino oscillation. The existence of one or more sterile neutrino flavours,  $\nu_s$ , could cause a deficit in the observed NC interaction rate. As with all the MINOS oscillation analyses, the energy spectrum of NC interactions observed in the ND (which was shown in Figure 8)

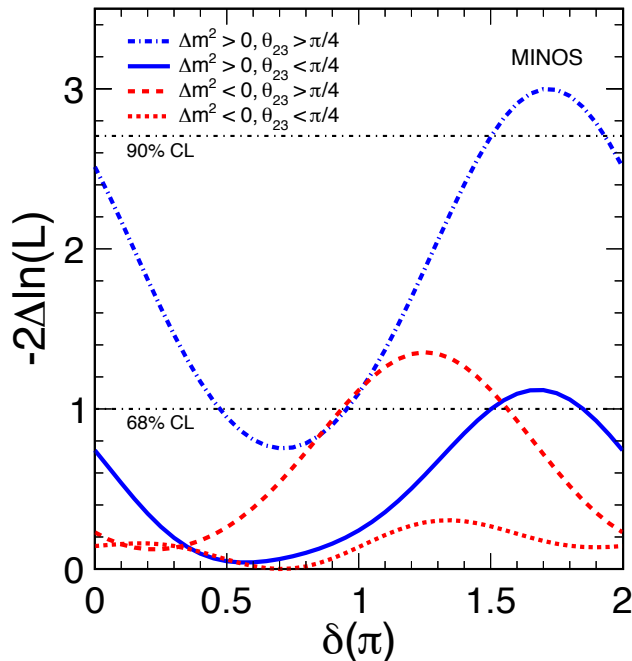


**Figure 18.** The values of likelihood  $L$  by which various values of the  $\mathcal{CP}$  violating parameter  $\delta$ , the mass hierarchy, and the octant of  $\theta_{23}$  are disfavoured.

is used to predict the spectrum expected at the FD [66]. The FD expectation is shown in Figure 19, with the dashed blue line taking into account  $\nu_e$  appearance corresponding to  $\theta_{13} = 11.5^\circ$  (at the limit set by CHOOZ [67], and a little above the current accepted value [26, 68–71]). The data are also shown in the figure, and are in good agreement with the expectation, confirming the standard model of neutrino oscillation.

The limit on the coupling of sterile to active neutrinos can be quantified by defining  $f_s$ , the fraction of disappearing  $\nu_\mu$  which have oscillated into  $\nu_s$ :

$$f_s = \frac{P_{\nu_\mu \rightarrow \nu_s}}{1 - P_{\nu_\mu \rightarrow \nu_\mu}}. \quad (7.1)$$

Assuming  $\theta_{13} = 11.5^\circ$ , MINOS limits  $f_s < 0.40$  at the 90% confidence limit.

## 8 The Future: MINOS+

The MINOS experiment has made some very important contributions to our understanding of neutrino oscillation physics, and has finished taking data with the beam for which it was designed. However, the experiment will continue taking data and producing new results for the next few years as MINOS+ [72]. The NuMI beam is being upgraded to a higher energy and intensity for the NO $\nu$ A experiment, the far detector of which will sit 14 mrad

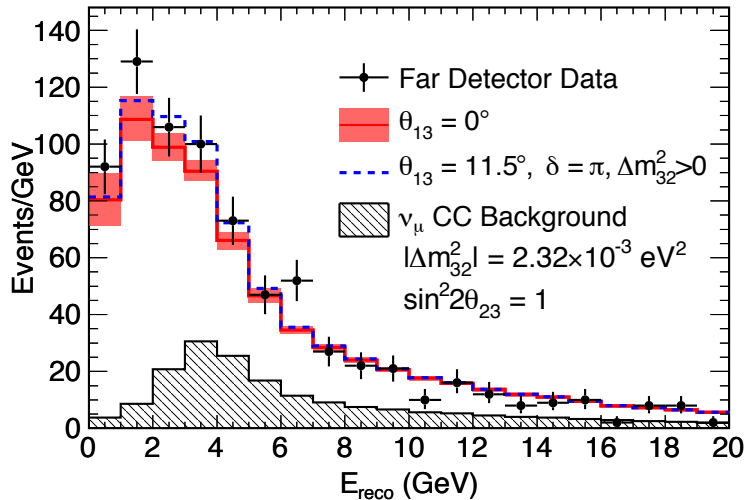


**Figure 19.** The black dots show the energy spectrum of NC interactions observed in the Far Detector. The red show the expectation in the case of no sterile neutrinos and  $\theta_{13} = 0$ ; the blue dashed line shows the same expectation with  $\theta_{13} = 11.5^\circ$ .

off-axis. NO $\nu$ A will receive a narrow-band beam, peaking at around 2 GeV, which is ideal for searching for  $\nu_e$  appearance since the background seen in MINOS from NC interactions of high energy neutrinos will be heavily reduced. Figure 20 shows that the MINOS FD will see an intense  $\nu_\mu$  beam, peaking at around 7 GeV. In this configuration, MINOS+ will observe around 4,000 CC  $\nu_\mu$  interactions in the FD each year; unprecedented statistics for a long-baseline oscillation experiment. This will offer a unique, high precision test of the three-flavour oscillation paradigm.

MINOS+ will be able to make a very sensitive search for the sterile neutrinos suggested by the LSND [73] and MiniBooNE [74] data, and by some interpretations of reactor neutrino data [75]. This search will cover more than three orders of magnitude in the mass splitting between the sterile and active neutrinos. The sensitivity of the MINOS+ experiment, when combined with the Bugey reactor neutrino data [76], is shown in Figure 21; MINOS+ has the potential to rule out much of the LSND allowed region.

## 9 Conclusion

The MINOS experiment was conceived at a time when neutrino oscillation had only recently been confirmed as the solution to the problem of neutrino flavour change. It has played a hugely influential role in bringing neutrino oscillation physics into an era of precision measurement. MINOS's measurement of the largest neutrino mass splitting is the most precise in the world. MINOS has made the first direct precision measurement of the corresponding antineutrino parameters, a measurement that promises to remain the world's most precise for many years. And MINOS has played a role in the discovery of a non-zero value for  $\theta_{13}$ .

Now that the value of  $\theta_{13}$  is known, the neutrino physics community can move on to determine the neutrino mass hierarchy, and to search for  $\mathcal{CP}$  violation in the neutrino sector.

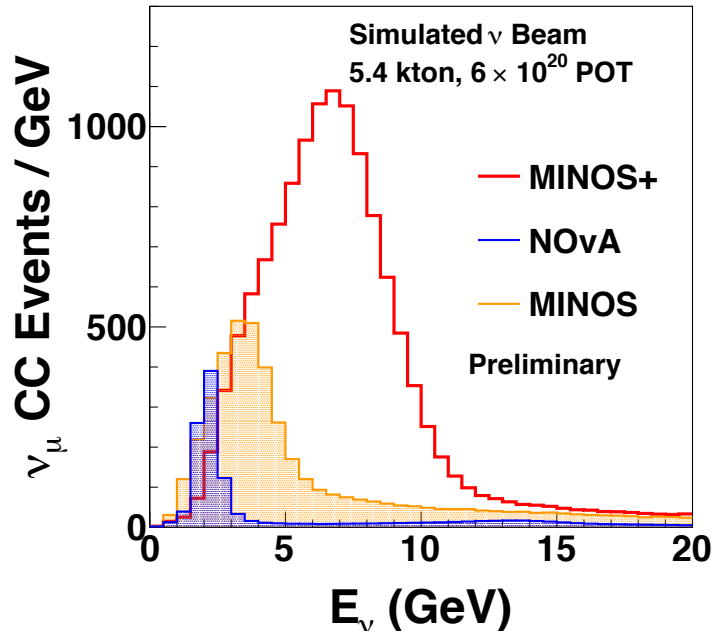


**Figure 20.** The  $\nu_\mu$  energy spectrum that will be observed by the MINOS+ FD, compared to the spectra observed by MINOS and NO $\nu$ A.

MINOS has pioneered a number of techniques that will be used by all future experiments. The two-detector setup, all important in reducing the impact of systematic uncertainties, is the design of choice for any new experiment; and MINOS has demonstrated methods of using a near detector to determine the expectation at a far detector. MINOS has performed the first search for  $\bar{\nu}_e$  appearance in a  $\bar{\nu}_\mu$  beam, and the first search for  $\nu_e$  and  $\bar{\nu}_e$  appearance with significant matter effects, demonstrating the analysis techniques that will be used to determine the mass hierarchy and  $\mathcal{CP}$  violation parameter.

In the second half of 2013, MINOS will begin taking data as the MINOS+ experiment, which will make ever more precise tests of the three-flavour neutrino oscillation paradigm and set world-leading limits on the existence of sterile neutrinos. This is an exciting future for an experiment that, with a decade of data taking so far, has already created a lasting legacy for itself in our understanding of the neutrino.

## Acknowledgments

The work of the MINOS and MINOS+ collaborations is supported by the US DoE, the UK STFC, the US NSF, the State and University of Minnesota, the University of Athens in Greece, and Brazil's FAPESP and CNPq. We are grateful to the Minnesota Department of Natural Resources, the crew of the Soudan Underground Laboratory, and the personnel of Fermilab, for their vital contributions.

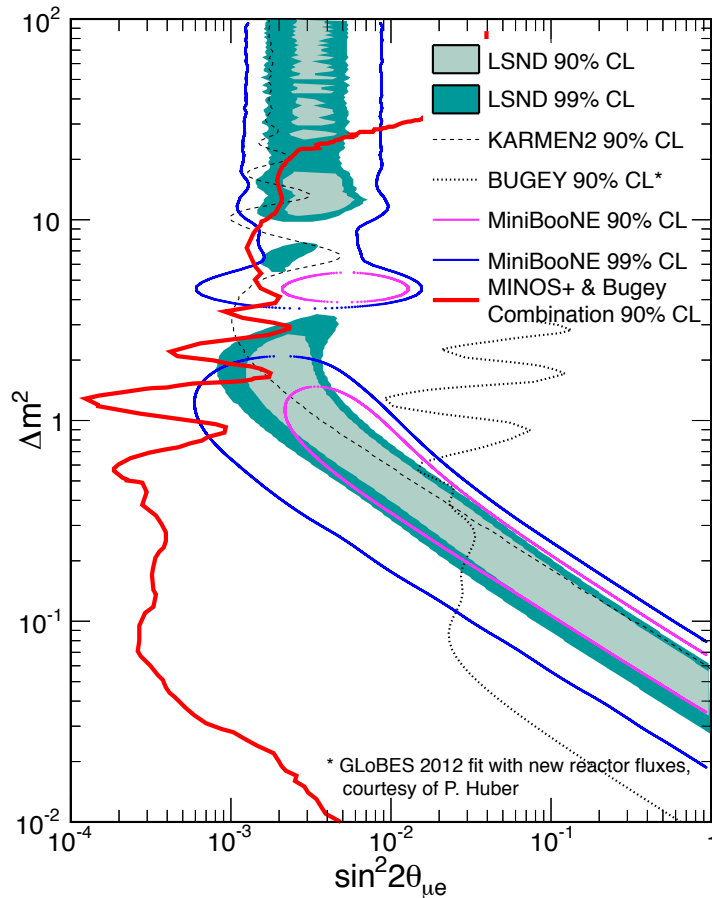


**Figure 21.** The sensitivity of MINOS+ to the existence of sterile neutrinos, when combined with data from the Bugey [76] reactor neutrino experiment.  $\Delta m^2$  is the splitting between the three known neutrino mass states and a new, fourth state.  $\theta_{\mu e}$  is the mixing angle governing  $\nu_{\mu} \rightarrow \nu_e$  transitions when a fourth, sterile neutrino state is introduced into the PMNS mixing matrix.

## References

- [1] S. Wojcicki, Nucl. Phys. Proc. Suppl. **77**, 182 (1999), proceedings of the XVIII International Conference on Neutrino Physics and Astrophysics (Neutrino 1998), Takayama, Japan, June 1998.
- [2] R. Davis, D.S. Harmer and K.C. Hoffman, Phys. Rev. Lett. **20**, 1205 (1968).
- [3] A.I. Abazov *et al.* (SAGE), Phys. Rev. Lett. **67**, 3332 (1991).
- [4] P. Anselmann *et al.* (GALLEX), Phys. Lett. **B285**, 376 (1992).
- [5] M. Aglietta *et al.* (NUSEX), Europhys. Lett. **8**, 611 (1989).
- [6] K. Hirata *et al.* (Kamiokande), Phys. Lett. **B280**, 146 (1992).
- [7] R. Becker-Szendy *et al.* (IMB), Phys. Rev. **D46**, 3720 (1992).

- [8] K. Daum *et al.* (Fréjus), Z. Phys. **C66**, 417 (1995).
- [9] S. Ahlen *et al.* (MACRO) Phys. Lett. **B357**, 481 (1995).
- [10] W. Allison *et al.* (Soudan2), Phys. Lett. **B391**, 491 (1997).
- [11] Y. Fukuda *et al.* (Super-Kamiokande), Phys. Rev. Lett. **81**, 1562 (1998).
- [12] Q.R. Ahmad *et al.* (SNO), Phys. Rev. Lett. **87**, 071301 (2001); Phys. Rev. Lett. **89**, 011301 (2002).
- [13] B. Pontecorvo, JETP **34**, 172 (1958); V.N. Gribov and B. Pontecorvo, Phys. Lett. **B28**, 493 (1969); Z. Maki, M. Nakagawa and S. Sakata, Prog. Theor. Phys. **28**, 870 (1962).
- [14] P. Adamson *et al.* (MINOS), Phys. Rev. Lett. **107**, 021801 (2011).
- [15] P. Adamson *et al.* (MINOS), Phys. Rev. **D84**, 071103 (2011).
- [16] P. Adamson *et al.* (MINOS), Phys. Rev. Lett. **108**, 191801 (2012).
- [17] P. Adamson *et al.* (MINOS), Phys. Rev. Lett. **110**, 251801 (2013).
- [18] K. Anderson *et al.*, FERMILAB-DESIGN-1998-01 (1998).
- [19] D.G. Michael *et al.* (MINOS), Phys. Rev. Lett. **97**, 191801 (2006).
- [20] P. Adamson *et al.* (MINOS), Phys. Rev. **D77**, 072002 (2008).
- [21] P. Adamson *et al.* (MINOS), Phys. Rev. Lett. **101**, 131802 (2008).
- [22] P. Adamson *et al.* (MINOS), Phys. Rev. Lett. **106**, 181801 (2011).
- [23] P. Adamson *et al.* (MINOS), Phys. Rev. Lett. **103**, 261802 (2009).
- [24] P. Adamson *et al.* (MINOS), Phys. Rev. **D82**, 051102 (2010).
- [25] P. Adamson *et al.* (MINOS), Phys. Rev. Lett. **107**, 181802 (2011).
- [26] P. Adamson *et al.* (MINOS), Phys. Rev. Lett. **110**, 171801 (2013).
- [27] P. Adamson *et al.* (MINOS), Phys. Rev. Lett. **101**, 221804 (2008).
- [28] P. Adamson *et al.* (MINOS), Phys. Rev. **D81**, 052004 (2010).
- [29] P. Adamson *et al.* (MINOS), Phys. Rev. Lett. **107**, 011802 (2011).
- [30] Ž. Pavlović, PhD thesis, University of Texas at Austin (2008).
- [31] F. Ballarini *et al.* (Fluka), J. Phys. Conf. Ser. **41**, 151 (2006).
- [32] S. Agostinelli *et al.* (GEANT4), Nucl. Instrum. Meth. **A506**, 250 (2003).
- [33] G. Battistoni *et al.* (Flugg), AIP Conf. Proc. **896**, 31 (2007).
- [34] D. Michael *et al.* (MINOS), Nucl. Instrum. Meth. **A596**, 190 (2008).
- [35] P. Adamson *et al.* (MINOS), Phys. Rev. **D73**, 072002 (2006).
- [36] P. Adamson *et al.* (MINOS), Phys. Rev. **D75**, 092003 (2007).
- [37] P. Adamson *et al.* (MINOS), Phys. Rev. **D86**, 052007 (2012).
- [38] M.A. Kordosky, PhD thesis, University of Texas at Austin (2004).
- [39] P.L. Vahle, PhD thesis, University of Texas at Austin (2004).
- [40] C. Backhouse, DPhil thesis, University of Oxford (2011).
- [41] T.M. Cover and P.E. Hart, IEE Trans. Inform. Theory **13**, 21 (1967).

- [42] R. Ospanov, PhD thesis, University of Texas at Austin (2008).
- [43] J.S. Marshall, PhD thesis, University of Cambridge (2008).
- [44] J.P. Ochoa, PhD thesis, Caltech (2009).
- [45] R. Toner, PhD thesis, University of Cambridge (2011).
- [46] A. Holin, PhD thesis, University College London (2010).
- [47] J. Boehm, PhD thesis, Harvard University (2009).
- [48] G. Tinti, DPhil thesis, University of Oxford (2010).
- [49] J.J. Evans, DPhil thesis, University of Oxford (2008).
- [50] S.J. Coleman, PhD thesis, College of William & Mary (2011).
- [51] J.S. Mitchell, PhD thesis, University of Cambridge (2011).
- [52] A. McGowan PhD thesis, University of Minnesota (2007).
- [53] M. Strait, PhD thesis, University of Minnesota (2010).
- [54] Y. Itow, in the proceedings of the XXV International Conference on Neutrino Physics and Astrophysics (Neutrino 2012), Kyoto, Japan, June 2012, to be published in Nucl. Phys. **B**.
- [55] K. Abe *et al.* (T2K), Phys. Rev. **D85**, 031103 (2012).
- [56] K. Nakamura *et al.* (Particle Data Group), J. Phys. **G37**, 075021 (2010). See pages 89 and 759.
- [57] L. Wolfenstein, Phys. Rev. **D17**, 2369 (1978).
- [58] J.W.F. Valle, Phys. Lett. **B199**, 432 (1987).
- [59] M.C. Gonzalez-Garcia *et al.*, Phys. Rev. Lett. **82**, 3202 (1999);
- [60] A. Friedland, C. Lunardini and M. Maltoni, Phys. Rev. **D70**, 111301 (2004).
- [61] Z. Isvan, PhD thesis, University of Pittsburgh (2012).
- [62] W.A. Mann *et al.*, Phys. Rev. **D82**, 113010 (2010).
- [63] J. Kopp *et al.*, Phys. Rev. **D82**, 113002 (2010).
- [64] J.A.B. Coelho, PhD thesis, Universidade Estadual de Campinas (2012).
- [65] A. Schreckenberger, PhD thesis, University of Minnesota (2013).
- [66] D.J. Koskinen, PhD thesis, University College London (2009).
- [67] M. Apollonio *et al.* (CHOOZ), Eur. Phys. J. **C27**, 331 (2003).
- [68] F.P. An *et al.* (Daya Bay), Chin. Phys. **C37**, 011001 (2013).
- [69] S-B Kim *et al.* (RENO), Phys. Rev. Lett. **108**, 191802 (2012).
- [70] Y. Abe *et al.* (Double Chooz), Phys. Rev. **D86**, 052008 (2012).
- [71] K. Abe *et al.*, arXiv:1304.0841 (2013).
- [72] G. Tzanakos *et al.*, FERMILAB-PROPOSAL-1016 (2011).
- [73] A. Aguilar *et al.* (LSND), Phys. Rev. **D64**, 112007 (2001).
- [74] A.A. Aguilar-Arevalo *et al.* (MiniBooNE), Phys. Rev. Lett. **103**, 111801 (2009); Phys. Rev. Lett. **110**, 161801 (2013).

- [75] G. Mention *et al.*, Phys. Rev. **D83**, 073006 (2011).
- [76] Nucl. Phys. **B434**, 503 (1995). The Bugey limit has been recomputed by P. Huber, accounting for the new reactor flux calculations used in [75].